Journal of Orthopaedic Research®

Journal of Orthopaedic Research®

RESEARCH ARTICLE

3D Morphometric Analysis of Femoral Isthmus Dimensions and Their Influence on Modular Kinked Revision Stem Design in Total Hip Arthroplasty

Marco Zucchet[1] | Cristiano Pizzamiglio[1] | Beat Schmutz[2,3,4,5] | Chong Bum Chang[6] | Jung-Wee Park[6] | Michele Pressacco[1]

[1]Global Research and Development Department, Villanova di San Daniele del Friuli, Italy | [2]Jamieson Trauma Institute, Brisbane, Australia | [3]School of Mechanical, Medical and Process Engineering, Faculty of Engineering, Queensland University of Technology, Kelvin Grove, Australia | [4]Centre for Biomedical Technologies, Queensland University of Technology, Kelvin Grove, Australia | [5]5ARC Training Centre for Multiscale 3D Imaging, Modelling, and Manufacturing, Queensland University of Technology, Kelvin Grove, Australia | [6]Department of Orthopaedic Surgery, Seoul National University Bundang Hospital, Seongnam-si, South Korea

Correspondence: Cristiano Pizzamiglio (cristiano.pizzamiglio@enovis.com)

Received: 27 February 2025 | **Revised:** 4 July 2025 | **Accepted:** 10 July 2025

Funding: LimaCorporate (now Enovis) provided funding for the acquisition of the CT images used in the study. B.S. received funding from LimaCorporate (now Enovis) for an initial pilot morphometric analysis. M.Z., C.P. and M.P. are employees of LimaCorporate (now Enovis). B.S. and C.B.C. provided and/or provide LimaCorporate (now Enovis) with consulting services.

Keywords: Bayesian inference | femoral axis | femoral isthmus | femoral revision stem | statistical shape model

ABSTRACT

The development of stems for femoral revision surgeries requires an understanding of how distal fixation can be achieved, especially in those cases where the curvature of the diaphysis is not negligible, and a straight stem could result in three-point fixation. To this extent, a series of parameters linked to the femoral canal isthmus were identified and their correlation, as well as the potential difference between White and Asian ethnicities, were investigated. The anatomical features of 215 three-dimensional femur models were automatically computed. Statistical inference was performed leveraging the frequentist and Bayesian frameworks. A moderate positive correlation was found between the three-dimensional proximal-isthmus axis angle α and the distance between the isthmus cross-section and proximal-isthmus axis tilting point D_{TI} ($p < 0.001$, $B_{10} = 1.1 \cdot 10^5$, $\rho = 0.35$). White subjects had both significantly longer distance between the head center and isthmus cross-section D_{HI} ($p < 0.001$, $B_{10} = 626.57$, $\Delta\mu = 10.18$ mm) and longer distance between the head center and tilting point D_{HT} ($p < 0.001$, $B_{10} = 1.2 \cdot 10^5$, $\Delta\mu = 12.33$ mm) with respect to Asian ones. Among all parameters, the correlation between α and D_{TI} is the most relevant and should be considered in designing a kinked revision stem to determine the best trade-off between fixation area and mechanical stability. The difference between White and Asian patients found for D_{HI} and the correlation between α and D_{HI} might have no practical effect in case of modular stem design. The remaining parameters had neither statistically significant correlation/difference nor practical impact on the design. These findings allow to reduce the design variables, thus leading to a more effective design process.

1 | Introduction

Total hip arthroplasties last 25 years in around 58% of patients [1]. Between 2003 and 2021, the Australian National Joint Replacement Registry alone, has recorded 83,206 hip revision arthroplasties, of which replacing the femoral component accounted for 19.5% (16,225) [2]. The most common complications of a first revision involving a fluted tapered modular

component in patients with extensive proximal femoral bone loss have been reported as postoperative instability (19%) and intra-operative femoral fracture during insertion of the stem (12%) [3]. These data highlight the need to develop prosthetic solutions that better match the anatomical characteristics and improve stability, aiming to reduce complications and enhance long-term outcomes in patients undergoing femoral revision surgery.

The focus of the current literature on the morphology of the proximal femoral metaphysis [4–7] is the design of femoral stems for primary total hip arthroplasty [8].

However, the development of stems for revision surgeries requires an understanding of how to properly anchor the lower portion of a hip replacement stem within the femoral bone to ensure stability and prevent loosening. Currently, the standard solution to distal fixation consists in designing tapered stems having either a straight, curved, or kinked geometry. Ensuring a true press-fit fixation, while avoiding a three-point one, can lead to better clinical outcomes [9]. To avoid three-point fixation, the axis of the distal portion of the stem should be aligned to the axis of the medullary canal region where fixation is achieved [10]. Indeed, if the curvature of the diaphysis is not negligible, the morphology of the canal cannot be modeled by a single geometrical axis, but a distinction between a proximal and an isthmus axis must be considered (Figure 1). If the diaphyseal curvature is negligible, then the three-dimensional angle (i.e., not projected onto a specific anatomical plane) between the proximal and isthmus axes α is negligible as well, thus a straight stem can achieve fixation. On the contrary, if α increases, a kinked design would be a better option, not only to achieve distal fixation, but also to avoid impingement in the greater trochanter region, since the proximal axis of the stem can potentially align to the proximal axis of the medullary canal. Furthermore, the intersection point between the proximal and isthmus axes (tilting point) is critical for designing kinked stems. As a result, the distances from the tilting point to both the isthmus section (D_{TI}) and the head center (D_{HT}) need to be taken into account. The distance between the head center and the isthmus (D_{HI}) is also important, as it helps evaluate the maximum stem length, given that a longer stem is more likely to achieve fixation at the isthmus level.

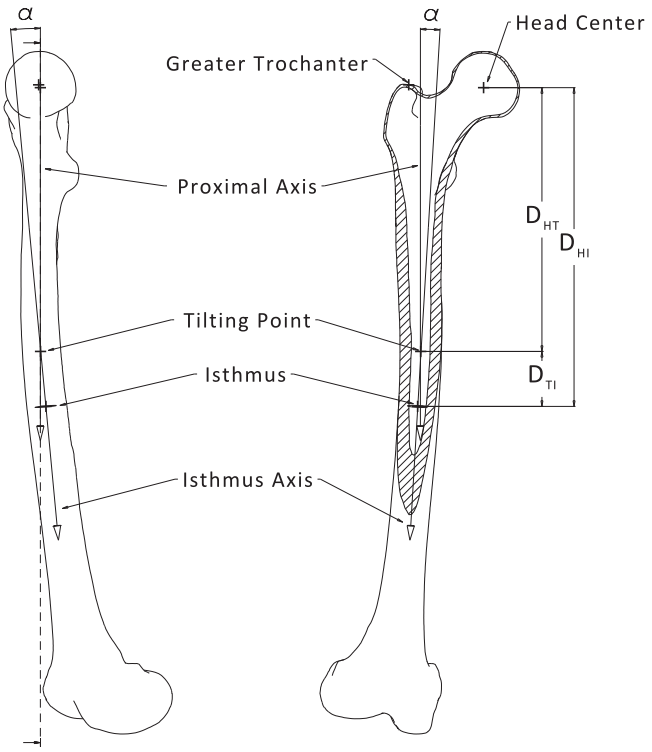

FIGURE 1 | Parameters of interest for the present study: the three-dimensional angle between the proximal and isthmus axes α, the distance between the isthmus cross-section and proximal-isthmus axis tilting point D_{TI}, the distance between the head center and isthmus cross-section D_{HI} and the distance between the head center and tilting point D_{HT}. The proximal and isthmus axes and the proximal isthmus axis tilting point are shown as well as the isthmus cross-section, head center and greater trochanter landmark. The distances D_{HI}, D_{TI} and D_{HT} are projected along the proximal axis.

1.1 | Related Work

The literature review concerning the isthmus tube and axis was conducted based on the query provided in the Supplementary File 1. Only one three-dimensional study was found in which the axis of the isthmus was defined as the axis of the isthmus tube [11]. The latter was computed as the set of inscribed circles near the canal isthmus and having diameters exceeding the isthmus diameter by up to 1.0 mm. The same methodology for the calculation of the isthmus tube was cited and adopted by Chen et al. [12]. In the present work, we propose a different methodology for the computation of the isthmus tube which relies on a relative threshold to better accommodate variations in femur size; moreover, in this study only the proximal region of the isthmus tube is considered. The definition of the femoral isthmus is a challenging task, especially for Dorr Type C [13] bone morphologies (also known as stovepipes) which may have multiple cross-sections with approximately the same area. For this reason, the isthmus was not identified as the minimum area cross-section similarly to other studies [4, 10, 11, 14], but by developing a more robust methodology. Regarding the definition of the medullary canal axes, different approaches are proposed in literature [6, 14–19]. For instance, Mahaisavariya et al. computed the proximal and distal axes by fitting the centers of the shaft's circular cross-sections on the proximal and distal sides of the isthmus section, respectively [14, 20]. Shimosawa et al. adopted an approach similar to the previous one; however, elliptical cross sections were computed, and the proximal and distal axes were calculated by fitting the centers of the ellipses on the proximal and distal halves of the shaft, respectively [15]. In the present work, an automated procedure is proposed to calculate the transition region between the two anatomical axes, rather than assuming its location a priori (e.g., isthmus cross-section).

Given the existing gap in the literature concerning the dimensional characteristics of the femoral isthmus needed for the design of modular kinked stems, this study aims to investigate whether α, the angle between the proximal and isthmus axes, correlates with the distances D_{HI}, D_{TI} and D_{HT}, and whether ethnicity (Asian vs White) might influence the design of kinked stems in terms of the above parameters (Figure 1) as studies

have shown differences in the femoral anterior bow radius between Asian and White patients [21, 22].

2 | Materials and Methods

The implemented methodology workflow, from data acquisition to the computation of α, D_{HI}, D_{TI}, and D_{HT}, is displayed in Figure 2. Unless otherwise stated, the steps in the workflow were performed using Figura by LimaCorporate (now Enovis), a proprietary research and implant development tool, which consists of three components: a database of anonymized CT images and bone models; a library, which leverages open-source software, for morphometric analyses, cortical bone mapping and quantitative computed tomography; and CAD software plug-ins for automatic virtual surgeries.

2.1 | A Priori Power Analysis and Data Collection

Considering a balanced two-tailed independent samples *t*-test, the calculation of the sample size per group requires the significance level α (0.05), the desired statistical power (0.80 [23–25]), and the Cohen's effect size δ, which was computed by adopting the formula reported by Cohen [23]. A value of 0.55 for δ was calculated based on the distance between the greater trochanter and isthmus cross-section D_{GI} for both Asian and White subjects provided in literature [10] and reported in Table 1. The computed minimum required sample size for each group is 53.

A total of 215 right adult femur models (60 Asians, 155 Whites) available in the database were analysed. With these sample sizes, a posterior power analysis reveals that an effect size $\delta \geq 0.55$ can be detected with a probability of at least 95%.

The Asian femurs were segmented from CT images of living donors, whereas the White ones from images of fresh-frozen postmortem specimens. The CT images have a slice thickness equal to either 1.0 or 2.0 mm, pixel size ranging from 0.58 to 0.80 mm, and only fully scanned femurs with no radiological artifacts were included. Femurs with deformities, traumas, tumors or in situ hardware were excluded from the study.

TABLE 1 | Computation of the effect size δ for the a priori power analysis based on the greater trochanter-isthmus distance D_{GI} for Asian and White subjects provided in literature [11]. The table reports sample size, mean and standard deviation for the two ethnicities. The last two columns show the pooled standard deviation σ_{pooled} and the resulting δ.

	Asian ($n = 369$)	**White ($n = 818$)**	σ_{pooled}	δ
D_{GI} (mm)	173 ± 23	185 ± 21	21.64	0.55

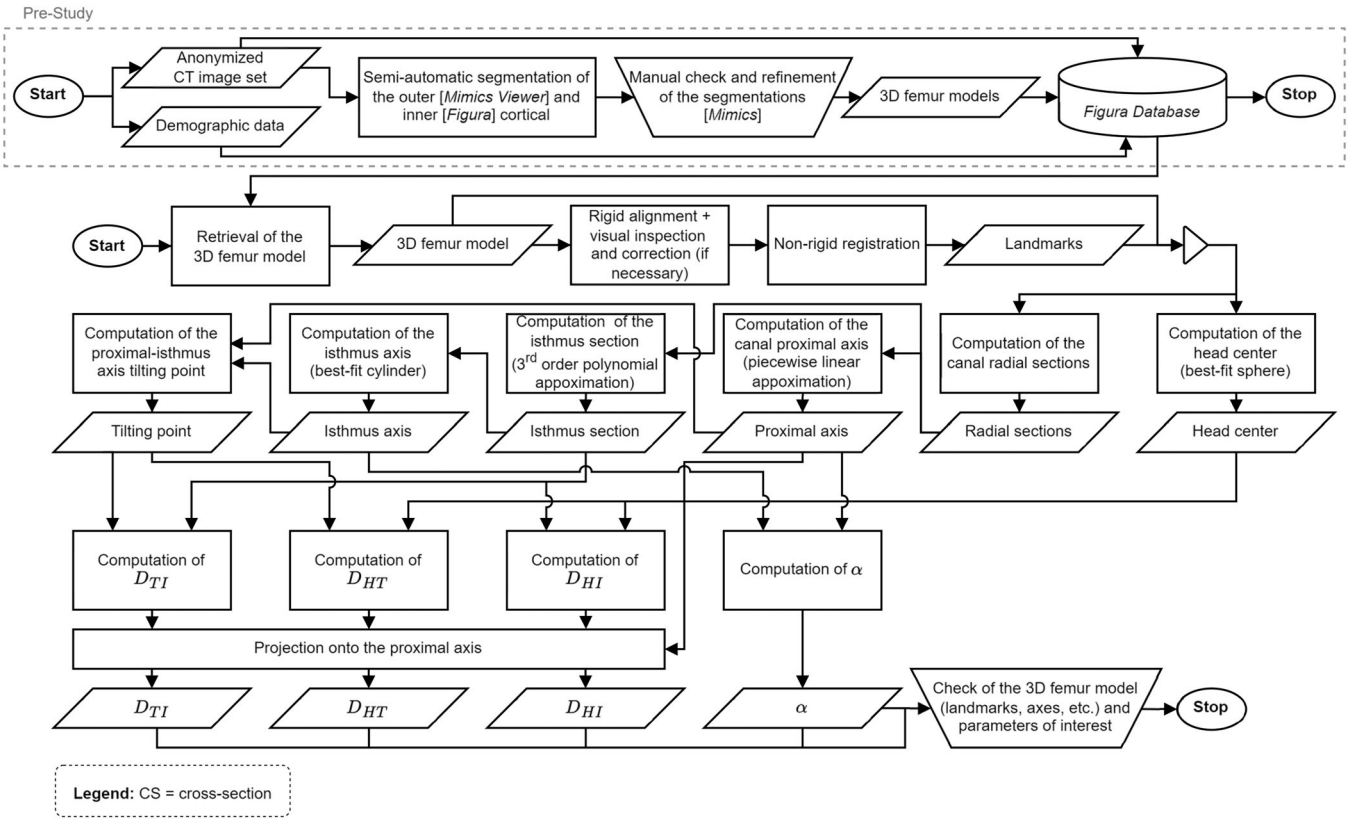

FIGURE 2 | Methodology workflow. The collection, segmentation and storage of the CT images was performed before the definition of the present study as denoted by the block labeled as pre-study. After the calculation of the minimum required sample size, all the three-dimensional nonpathological femur models available in the Figura database were retrieved. The femur models and the landmarks were used to compute the parameters of interest, that is, α, D_{HI}, D_{TI}, and D_{HT}.

2.2 | Ethics Approval and Consent to Participate

Informed consent was obtained from all individual participants included in the study. Specifically, CT images and demographic data were collected from different sites with approval of the local ethics committees. 115 CT images of postmortem White specimens were acquired from the body donation organization Science Care (Science Care Inc. Phoenix, Arizona, USA), which declared that written informed consent was obtained for all donors on which imaging was performed, and the remaining 40 CT images of White donors were acquired from the body bequest program of the Queensland University of Technology (QUT, Brisbane, Australia) upon approval of the QUT University Human Research Ethics Committee (QUT UHREC, Reference number: 2000001080). CT images of living Asian donors were provided by the Seoul National University Bundang Hospital (SNUBH, Seoul, South Korea) upon approval of the SNUBH Institutional Review Board (SNUBH IRB, IRB No. B-2111-721-102). This study was performed in line with the principles of the Declaration of Helsinki.

2.3 | Automatic Segmentation

The periosteal bone cortex boundary was automatically segmented using the cloud-based Mimics Viewer (Materialise, Leuven, Belgium) which leverages thresholding, deep learning, graph-based and model-based segmentation algorithms. The endosteal boundary was automatically segmented using a validated deconvolution algorithm based on the cortical bone mapping technique [26–28] implemented into Figura. The segmentations were all inspected by the same experienced engineer and minor corrections were applied when necessary using Mimics (Materialise, Leuven, Belgium) and its Edit Contours tool. Bone meshes were generated using the Calculate Part tool, available in Mimics, by setting its quality parameter to optimal. To increase the accuracy of the automatic landmark detection algorithm described in the following section, the triangular mesh of the bone models was remeshed using the isotropic explicit remeshing algorithm [29] available in Meshlab (National Research Council, Italy) [30]. The average edge length of the surface meshes is 1.89 ± 0.25 mm.

2.4 | Automatic Landmark Detection

The manual identification of landmarks in a large data set of bones is a time-consuming task and prone to user variability. Thus, an automatic methodology was implemented which consists of two main steps: rigid alignment and correspondence establishment. Since only non-pathologic and fully scanned femurs were considered, the normalization of their pose was achieved by aligning their principal axes of inertia to a common coordinate system. The alignment results were visually inspected using a custom-built application, which displays each shape sequentially. Then, shapes in correspondence were created by selecting a reference femur which is non-rigidly registered onto the other shapes, also known as target shapes. The result is a set of shapes having the same number of nodes which are mapped to the nodes of the reference femur. The nonrigid registration was performed using the open-source library Scalismo [31], which is a Figura dependency. To prevent potential bias, the nonrigid registration was performed twice similarly to the procedures described in literature [32, 33]. From the first iteration, a statistical shape model (SSM) was created using the principal component analysis and the resulting average femur was used as reference for the second registration. Nine landmarks were mapped from the surface of the average shape stemming from the second SSM to the target femurs as illustrated in Figure 3 (left): tip of the greater trochanter [34]; five points over the anterior, posterior, medial, lateral and superior aspects of the femoral head; a point located at the distal base of the lesser trochanter, marking the proximal end of the diaphysis; a point on the medial aspect of the distal diaphysis marking the distal end of the diaphysis [21]; the saddle point located at the distal region of the intercondylar fossa [22].

2.5 | Medullary Canal Radial Cross-Sections Computation

The diaphyseal inner cortical boundary was initially subdivided into forty equally spaced parallel [21, 35] cross-sections, which extend from the proximal to the distal construction points of the diaphysis, and whose normal vector lies on the axis passing through the tip of the greater trochanter and the distal

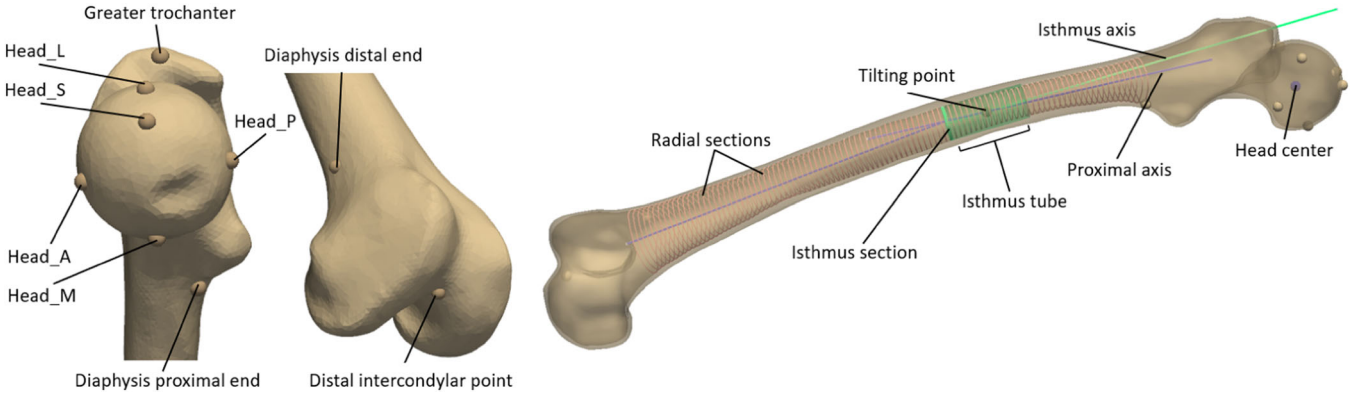

FIGURE 3 | The landmarks used for the analysis (left): tip of the greater trochanter, five points over the anterior, posterior, medial, lateral and superior aspects of the femoral head, proximal and distal end of the diaphysis, and a point located in the distal region of the intercondylar fossa. Automatically computed geometrical entities (right): three-dimensional model of a femur where the proximal canal axis, isthmus axis, isthmus cross-section, isthmus tube, proximal-isthmus axis tilting point, head center, radial cross-sections and landmarks are displayed.

intercondylar point. The centroids of the parallel cross-sections were used to calculate a three-dimensional best-fit circle. The latter served as a guide to define one hundred equiangular radial cross-sections allowing for a better modeling of the femoral shaft curvature. The span of the radial cross-sections is defined by the best-fit circle arc delimited by the proximal and distal construction points of the diaphysis.

2.6 | Medullary Canal Axes Computation

The radial cross-sections' centroids were utilized to compute the proximal and distal canal axes by running a piecewise linear approximation where the breakpoint, that is, one of the centroids that acts as the transition point between the two axes, was automatically located by minimizing the overall approximation error (OAE). The latter was calculated as a weighted root mean square error using the following formula:

$$OAE = \sqrt{\frac{n_P \cdot RMSE_P^2 + n_D \cdot RMSE_D^2}{n_P + n_D}},$$

where n_P and n_D are the number of centroids involved in the computation of the proximal and distal best-fit axes respectively, and $RMSE_P$ and $RMSE_D$ are the corresponding root mean square errors. The optimal canal axes were computed by running an iterative procedure as shown in Figure 4 (left). In each iteration, the proximal best-fit axis was computed with a proximal subset of contiguous radial cross-section centroids, and the distal best-fit axis with the remaining centroids. Then, the corresponding OAE was computed and compared with the OAE of the previous iteration; if the latest OAE is lower than the previous one, then the optimal canal axes are updated. The procedure was repeated by adding one centroid to the proximal subset and thus by removing one to the distal subset. The minimum number of centroids in the subsets was set to one fourth of the total number of centroids. The optimal canal axes and the breakpoint are depicted in Figure 4 (right).

2.7 | Isthmus Cross-Section and Axis Computation

The areas of the radial cross-sections were modeled with a best-fit cubic polynomial, which was considered to be a good trade-off between under- and overfitting the data points. The minimum of the polynomial allowed to identify the cross-section index corresponding to the isthmus. Then, the polynomial was scaled by its value computed at the isthmus index and the axis of the latter was defined as the axis of the best-fit cylinder spanning from the isthmus cross-section itself to the proximal cross-section having scaled area 10% greater than the isthmus area. To the extent of the authors' knowledge, only two studies found in literature computed the isthmus tube using a three-dimensional methodology [11, 12]. In both studies, a fixed 1.0 mm diameter difference threshold, relative to the isthmus cross-section, was used to identify the cross-sections comprising the tube. Instead, in the present work a relative threshold of 10% was adopted to better accommodate variations in femur size.

2.8 | Computation of α, D_{HI}, D_{TI} and D_{HT}

The three-dimensional angle α was computed as the angle between the proximal and isthmus axes. D_{HI} was computed as the distance between the head center and isthmus cross-section, D_{TI} as the distance between the isthmus cross-section and proximal-isthmus axis tilting point, while D_{HT} as the distance between the head center and the proximal-isthmus axis tilting point. The head center was computed as the center of the sphere that best-fits the five landmarks over the femoral head, while the proximal-isthmus axis tilting point was defined as the

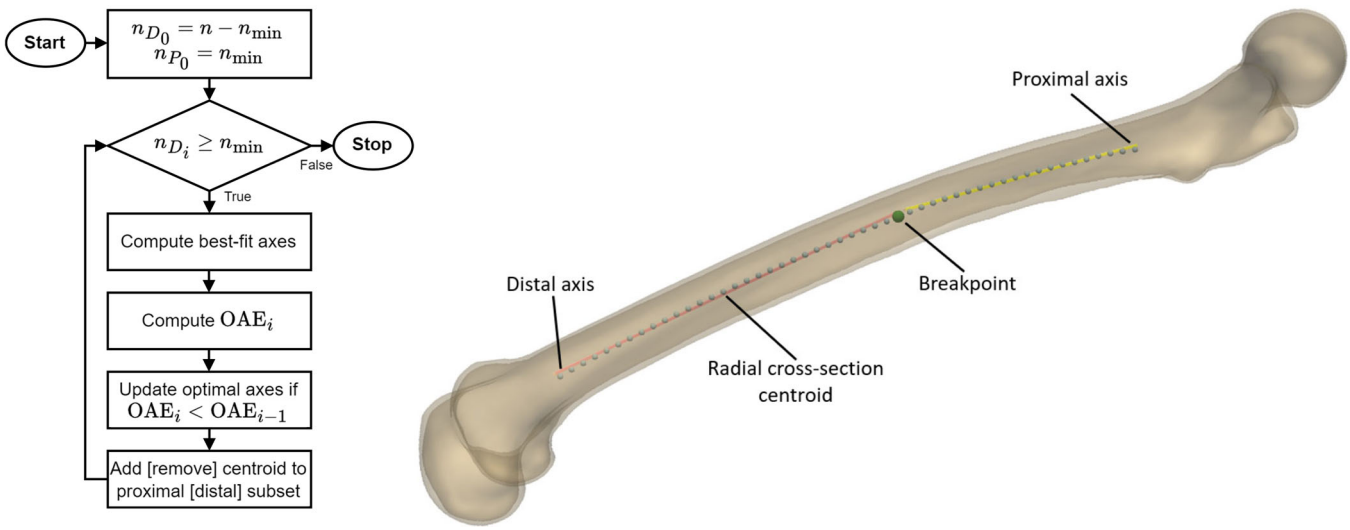

FIGURE 4 | Medullary canal axes computation. Flowchart of the procedure where n_{P0} and n_{D0} are the number of radial cross-section centroids allocated to the proximal and distal subsets in the first iteration, n is the total number of centroids, n_{min} is the minimum number of centroids allowed in both subsets, and OAE is the overall approximation error (left). The optimal proximal and distal canal axes are shown together with the radial cross-section centroids and the breakpoint of the piecewise linear approximation. For visual clarity, only fifty centroids are displayed (right).

point closest to both axes. In this study, it is also proposed to project the distances over the proximal axis, which serves as a reference axis, ensuring that distances are consistently measured relative to a standardized direction, thus making the results easier to compare across different individuals and studies. Finally, the detected landmarks, the geometrical features (i.e., axes, planes, etc.) and the numerical values of the parameters of interest were all checked. No errors were detected across the whole sample.

2.9 | Data Analysis

The reliability of the proposed methodology for the computation of the parameters of interest was assessed by computing intraclass correlation coefficients. Two experienced orthopedic engineers, referred also as observers, each picked the landmarks five times [33] using a custom-made graphical user interface. A two-way random effects, absolute agreement, and single measurement model was used for evaluating the interobserver reliability, whereas the intra-observer reliability was assessed with a two-way mixed effects, absolute agreement, and single measurement model [33, 36]. For both models, a sample size calculation revealed that at least 10 femurs needed to be processed by the engineers, based on an estimated sample intraclass correlation coefficient of 0.9, and a 95% confidence interval with a width 0.2 [36]. A random sample of twenty-one femurs was selected. The intraclass correlation coefficients were interpreted following the guidelines reported by Koo [37].

To assess the accuracy of the automatic landmark detection algorithm, the values of the parameters of interest derived from the automatically detected landmarks were compared to those obtained from the manually selected landmarks (the results from the two observers were averaged) by running the robust and non-parametric Passing-Bablok regression for method comparison [38]. Before running the test, the assumptions of linearity and high positive correlation were checked.

To provide a richer understanding of the data, frequentist inference is complemented by Bayesian hypothesis testing. Thus, in this study Bayes factors B_{10} are reported alongside p values. The Bayes factor is classified using the scheme suggested by Jeffreys [39] where a factor between 1 and 3 is considered negligible evidence, between 3 and 10 substantial evidence and a factor greater than 10 is regarded as strong evidence.

Correlations between the two groups were evaluated by running Pearson's correlation tests. Bayes factors are reported together with Pearson's correlation coefficients ρ and their 95% credibility intervals. The Pearson's coefficient is classified according to the general guidelines provided by Cohen [23], where a value less than 0.3 indicates a weak correlation and between 0.3 and 0.5 is regarded as moderate correlation.

Two-tailed independent samples t-tests were run to assess differences between the two ethnicities. Outliers, which were visually detected using boxplots, were all retained since they were deemed genuine and not due to processing errors. Before running the test, the normality of the dependent variables was tested both quantitatively, using the Shapiro-Wilk's test [40], and qualitatively by inspection of the quantile-quantile plots. If the normality assumption is violated, the non-parametric Mann-Whitney U test was run. The homogeneity of variances was assessed by running the Levene's test and if the homoscedasticity condition was not met, the Welch's t-test was run. Effect sizes and mean differences $\Delta\mu$ are reported to help evaluate the practical significance of the results. Furthermore, the prior and posterior distributions of the effect size are computed alongside its 95% credibility interval (CI). Robustness analyses of the Bayes factor are computed as well, which allow to assess how different prior distribution widths can affect the value of the factor. A Cauchy distribution having width equal to 0.707 was selected as the default prior [39, 41, 42].

Finally, a frequentist mediation analysis was performed to assess whether the effect of ethnicity on the distances of interest, that is, D_{HI}, D_{TI} and D_{HT}, is mediated by either the height or femur length of the patients. Standardized estimates β and their 95% confidence intervals are reported.

The Passing-Bablok regression was performed using the statistics software NCSS 22.0.3 (NCSS LCC, Utah, USA), and the mediation analyses using the open source software JASP 0.18.3.0 [43]. The latter was also used to compute the intraclass correlation coefficients, whereas the corresponding sample size calculation was performed using PASS 22.0.2 (NCSS LCC, Utah, USA). Power analyses, Pearson's correlation and independent samples tests were carried out using the open source software Jamovi 2.3.28 [44].

3 | Results

The intraclass correlation coefficients for both inter- and intra-observer reliability are reported in Table 2. The lower boundary of the 95% confidence interval of the intraclass correlation coefficients ranges from 0.913 to 0.992 for the interobserver

TABLE 2 | Values of the intraclass correlation coefficients for both inter- and intra-observer reliability and their 95% confidence intervals.

	Interobserver	Intraobserver - Observer 1	Intraobserver - Observer 2
α (deg)	0.994 [0.985, 0.997]	0.976 [0.956, 0.989]	0.968 [0.942, 0.985]
D_{HI} (mm)	0.992 [0.947, 0.998]	0.983 [0.969, 0.992]	0.972 [0.942, 0.988]
D_{HT} (mm)	0.988 [0.913, 0.996]	0.973 [0.950, 0.988]	0.968 [0.941, 0.985]
D_{TI} (mm)	0.988 [0.970, 0.995]	0.937 [0.888, 0.971]	0.916 [0.852, 0.960]
D_{GI} (mm)	0.997 [0.992, 0.999]	0.981 [0.963, 0.991]	0.969 [0.934, 0.987]

reliability, from 0.888 to 0.969 for the intra-observer reliability of Observer 1, and from 0.852 to 0.942 for the intra-observer reliability of Observer 2.

The validation results of the landmark detection algorithm are listed in the Supplementary File 2, which reports the slope and intercept values from the Passing-Bablok regression, along with their 95% confidence intervals.

The correlation results are summarized in Table 3. As shown in Figure 5 (left), there was a moderate positive correlation between the proximal-isthmus axis angle α and the tilting point-isthmus distance D_{TI} ($p < 0.001$, $B_{10} = 1.1 \cdot 10^5$, $\rho = 0.35$), with the angle explaining 12% of the distance variation. The 95% credibility interval of the correlation coefficient ranged from 0.23 to 0.46. A low positive correlation was found between the angle α and the head center-isthmus distance D_{HI} ($p < 0.001$, $B_{10} = 91.65$, $\rho = 0.25$), with the angle α explaining 6% of the distance variation as depicted in Figure 5 (right). The 95% credibility interval of the correlation coefficient ranged from 0.12 to 0.37. The angle α and head center-tilting point distance D_{HT} were not significantly correlated ($p = 0.92$, $B_{10} = 0.09$, $\rho = 0.01$). In addition, the correlations between the femur length and both D_{HI} and D_{HT} were investigated. High correlations were found for both D_{HI} ($p < 0.001$, $\rho = 0.66$, 95% CI [0.58, 0.73]) and D_{HT} ($p < 0.001$, $\rho = 0.56$, 95% CI [0.46, 0.65]).

Figure 6 displays demographics data and distribution of the parameters of interest ethnicity-wise, while Table 4 reports the results of the independent samples tests, including the parametric *t*-test, its non-parametric counterpart, and the corresponding Bayes factors. Regarding the demographics data, practical significance differences were found in terms of height and BMI. White subjects were taller ($p < 0.001$, $B_{10} = 2.7\ 10^7$, $\Delta\mu = 0.09$ m, $\delta = 0.97$ with 95% CI [0.66, 1.28]) and had lower BMI ($p < 0.001$, $B_{10} = 244.88$, $\Delta\mu = 3.07\ \mathrm{kgm}^{-2}$, $\delta = 0.58$ with 95% CI [0.28, 0.89]). Age, weight and BMI violated the assumption of homogeneity of variances. Moreover, age was not normally distributed.

The three-dimensional angle between the proximal and isthmus axes α violated the normality assumption. No significant evidence was found to support the alternative hypothesis H_1 ($p = 0.054$, $B_{10} = 0.72$, $\Delta\mu = 0.42$ deg). A Bayes factor of 626.57 suggests strong evidence that the head center-isthmus distance D_{HI} was longer for White subjects ($p < 0.001$, $\Delta\mu = 10.18$ mm). Figure S1 (left) in the Supplementary File 3 shows that the median of the posterior distribution of δ is 0.62 with a 95%

TABLE 3 | Correlation results. The table reports *p*-value, Bayes factor B_{10} and Pearson's correlation coefficient ρ along with its 95% credible interval.

	p	$\mathbf{B_{10}}$	$\boldsymbol{\rho}$ **(95% CI)**
α versus D_{TI}	< 0.001	$1.1 \cdot 10^5$	0.35 [0.23, 0.46]
α versus D_{HI}	< 0.001	91.65	0.25 [0.12, 0.37]
α versus D_{HT}	0.92	0.09	0.01 [−0.13, 0.14]
Femur length versus D_{HI}	< 0.001	$>1.0 \cdot 10^5$	0.66 [0.58, 0.73]
Femur length versus D_{HT}	< 0.001	$>1.0 \cdot 10^5$	0.56 [0.46, 0.65]

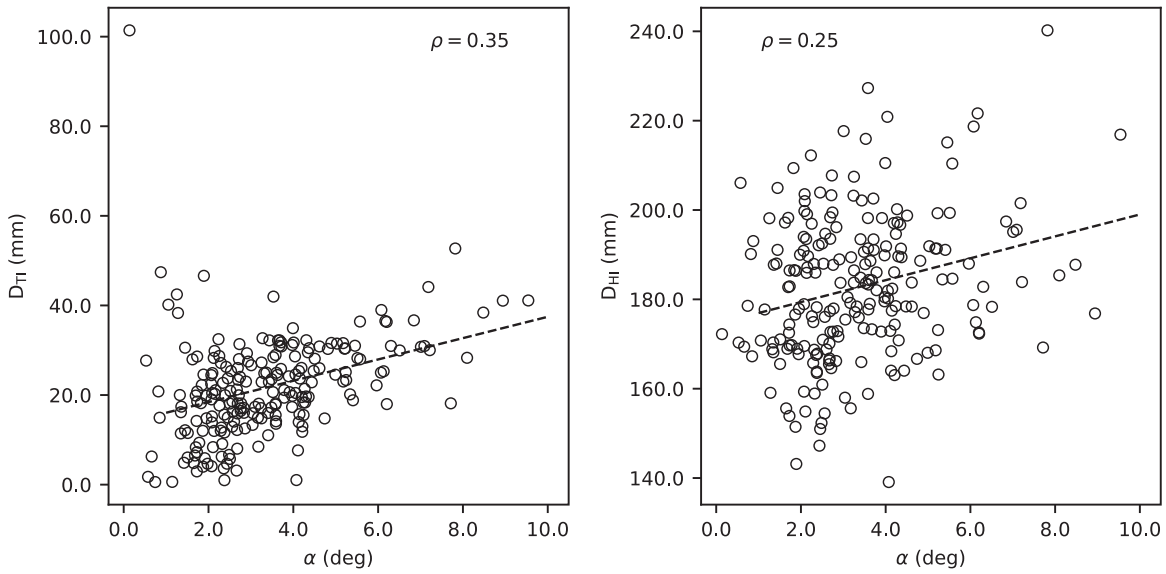

FIGURE 5 | Correlation plots. A Pearson's correlation coefficient of 0.35 shows a moderate correlation between α and D_{TI} (left), whereas between α and D_{HI} a low correlation of 0.25 was evaluated (right).

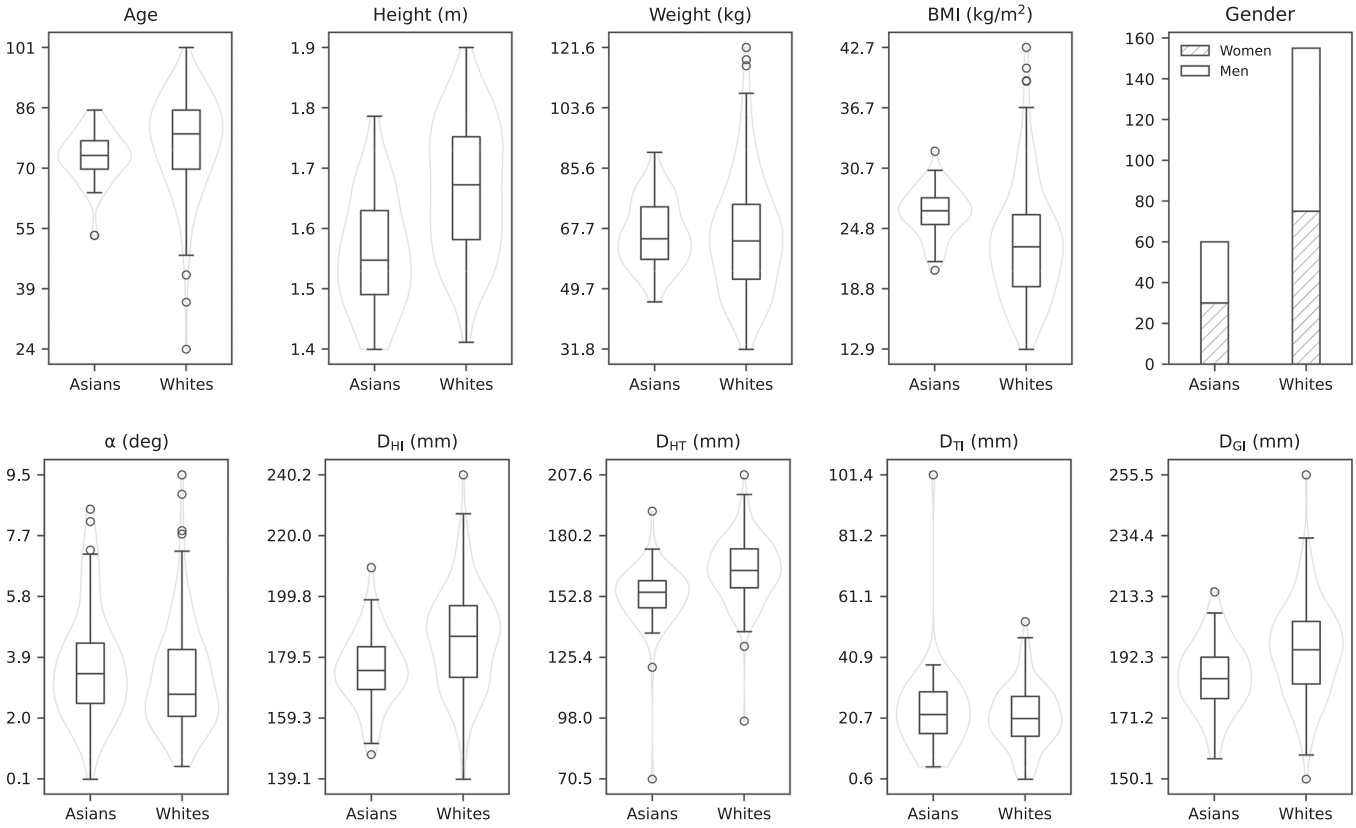

FIGURE 6 | Violin plots for age, height, weight, BMI, gender, α, D_{HI}, D_{HT}, D_{TI}, and D_{GI} ethnicity-wise.

TABLE 4 | Descriptive and inferential statistics results for age, height, weight, body mass index (BMI), gender, α, D_{HI}, D_{HT}, D_{TI} and D_{GI} ethnicity-wise. The table reports mean μ, standard deviation σ, mean difference $\Delta\mu$, p-value, Bayes factor B_{10} and median effect size δ along with its 95% credible interval.

	$\sigma \pm \mu$					
	Asians	**Whites**	$\Delta\mu$	p	B_{10}	δ **(95% CI)**
Age	73.03 ± 6.40	76.75 ± 12.42	−3.72	0.01	1.56	−0.31 [−0.61, −0.02]
Height (m)	1.58 ± 0.08	1.67 ± 0.10	−0.09	< 0.001	$2.7 \cdot 10^7$	−0.97 [−1.28, −0.66]
Weight (kg)	66.20 ± 9.76	65.64 ± 17.79	0.56	0.77	0.17	0.03 [−0.25, 0.31]
BMI (kg m^{-2})	26.38 ± 2.37	23.31 ± 5.72	3.07	< 0.001	244.88	0.58 [0.28, 0.89]
α (deg)	3.68 ± 1.75	3.23 ± 1.64	0.42	0.054	0.72	0.25 [−0.04, 0.54]
D_{HI} (mm)	175.38 ± 12.09	185.56 ± 16.85	−10.18	< 0.001	626.57	−0.62 [−0.93, −0.31]
D_{HT} (mm)	152.48 ± 15.11	164.81 ± 14.50	−12.33	< 0.001	$1.2 \cdot 10^5$	−0.81 [−1.12, −0.49]
D_{TI} (mm)	22.76 ± 13.76	21.23 ± 10.24	1.54	0.37	0.24	0.13 [−0.16, 0.42]
D_{GI} (mm)	185.38 ± 12.08	194.73 ± 16.25	−9.34	< 0.001	267.46	−0.58 [−0.89, −0.28]

credible interval ranging from 0.31 to 0.93. The robustness analysis depicted in Figure S1 (right) shows that the Bayes factor remained stable across different prior distribution widths. Asian patients had a shorter head center-tilting point distance D_{HT} ($p < 0.001$, $B_{10} = 1.2 \cdot 10^5$, $\Delta\mu = 12.33$ mm). The posterior distribution of the effect size had median equal to 0.81 (95% CI [0.49, 1.12]) as shown in Figure S2 (left) in the Supplementary File 3. Considering an ultra-wide prior distribution, the Bayes factor still suggested strong evidence in favor of H_1 as shown in Figure S2 (right). The tilting point-isthmus distance D_{TI} showed no practical significant difference ($p = 0.37$, $B_{10} = 0.24$, $\Delta\mu = 1.54$ mm). The distance between the greater trochanter and isthmus cross-section D_{GI} is not one of the main parameters investigated in this study, however D_{GI} results are reported as well since it was used for the sample size calculation. D_{GI} was statistically significant ($p < 0.001$, $B_{10} = 267.46$, $\Delta\mu = 9.34$ mm) and the posterior distribution of the effect size δ had median equal to 0.58 (95% CI [0.28, 0.89]); the posterior distribution and

robustness analysis for D_{GI} are reported in Figure S3 in the Supplementary File 3. For both D_{HI} and D_{GI} the assumption of homogeneity of variances was not met. For all the relevant parameters, the percentage error calculation of the Bayes factor was lower than 10%. Additional descriptive statistics, such as maximum, minimum, median, first and third quartile, for both demographics and parameters of interest are reported in the Supplementary Files 4 and 5 respectively.

A mediation analysis was run for D_{HI} and D_{HT}. Regarding D_{HI}, the direct effect of ethnicity was no longer significant after adding height to the mediation model ($p = 0.39$, $\beta = 0.12$, 95% CI [−0.15, 0.38]) and a statistically significant indirect effect was found ($p < 0.001$, $\beta = 0.51$, 95% CI [0.32, 0.69]). Similarly, for D_{HT} ($p = 0.004$, $\beta = 0.41$, 95% CI [0.13, 0.69]) a statistically significant indirect effect was found ($p < 0.001$, $\beta = 0.38$, 95% CI [0.22, 0.54]). A similar pattern emerged when patient height was replaced with femur length. Regarding D_{HI}, the direct effect of ethnicity was no longer significant after adding height to the mediation model ($p = 0.17$, $\beta = -0.18$, 95% CI [−0.44, 0.08]) and a statistically significant indirect effect was found ($p < 0.001$, $\beta = 0.81$, 95% CI [0.58, 1.03]). Similarly, for D_{HT} ($p = 0.18$, $\beta = 0.19$, 95% CI [−0.09, 0.48]) a statistically significant indirect effect was found ($p < 0.001$, $\beta = 0.59$, 95% CI [0.40, 0.79]).

4 | Discussion

The correlation analysis showed a moderate positive correlation between α and D_{TI} ($\rho = 0.35$); this implies that raising the kinking point of the stem with respect to the fixation area will result in an increased kinking angle. Considering that moving the kinking point distally can result in a reduction of fixation area length and increasing the kinking angle can increase the lever arm of the force applied to the implant, the optimal trade-off between kinking height and kinking angle should be carefully evaluated during the development of a kinked stem. The low correlation found between α and D_{HI} ($\rho = 0.25$) indicates that kinking angle could increase with total stem length. In case of modular stem design, the total construct length can be adjusted with the proximal body keeping the same stem length. For this reason, the impact of the correlation between α and D_{HI} should be evaluated depending on other design choices. No significant correlation was found for α and D_{HT} ($\rho = 0.01$) meaning that the kinking point height definition should not be based on the distance from the head center since this would result in no significant correlation with the kinking angle. The results of the statistical analysis for α and D_{TI} showed neither evidence of differences nor equivalence between White and Asian subjects; nevertheless, considering that the difference of the means of α is less than 0.5° ($\Delta\mu = 0.42°$), this will probably have little-to-no practical impact in the final design of a kinked stem. The same goes for D_{TI} since the difference in the means is $|\Delta\mu|$=1.54 mm. Both D_{HI} and D_{HT} were significantly longer for Whites with respect to Asians. Also in this case, together with the results of the statistical analysis, an evaluation of the practical effect on the stem design shall be considered: a difference in the means $|D_{HI}|$ of 10.18 mm could, in case of modular stem design, be addressed with a longer proximal body, keeping the same stem length for Asian and White subjects. Regarding D_{HT}, since no significant correlation with α was found, its dependency on ethnicity has no impact on the kinked stem design thus it can be neglected. Furthermore, the results of the mediation analyses showed that the effect of ethnicity on D_{HI} and D_{HT} is caused by differences in height between Asian and White patients.

Given the observed variability in parameters, it may be beneficial to expand the range of stem geometries to better fit individual anatomies. A 3D fitting analysis, including combinations with proximal bodies, could provide insights into the optimal number of implants needed. However, alongside anatomical fit, the impact on inventory, surgical instruments, and complexity should be considered, as more components could increase logistical challenges. To the best of the authors' knowledge, no existing literature defines two separate axes, namely the proximal canal and isthmus axes, and evaluates the angle α between them. Consequently, it was challenging to compare the results of this study with those in existing literature. As opposed to Bozkurt et al. [6], the medullary canal was modeled by defining a fixed number of equiangular radial cross-sections, thus enabling an analysis of the canal which is independent of the individual variation in femur length. Moreover, the medullary canal axes were computed by adopting an automatic methodology, which does not rely on defining a priori the transition region between the two anatomical axes, thus providing a more robust approach to accurately capture the natural variation in bone morphology and improving both the reliability and reproducibility of the analysis. In contrast to Su et al. [11] and Chen et al [12], the isthmus tube was computed by adopting a relative percentage threshold instead of an absolute one, to better account for differences in femur size; furthermore, only the proximal region of the isthmus tube was considered for the calculation of the isthmus axis.

Since the D_{GI} results reported by Thiesen et al. [10] were leveraged for calculating the sample size (Table 1), a comparison with the present study is proposed. Both studies observed a statistically significant difference between Asian and White patients with Asian subjects exhibiting a shorter D_{GI}. The mean differences reported by Thiesen et al. and the present work are 12.00 mm and 9.34 mm respectively. The D_{GI} values reported here are 7.16% and 5.26% higher for Asian and White patients compared to the respective values reported by Thiesen et al. This outcome can be attributed to the methodology adopted in this study for the calculation of the isthmus section, which relies on modeling the canal cross-sections with a best-fit cubic polynomial rather than identifying the minimum area cross-section. This is evident when the canal morphology exhibits multiple cross-sections of comparable area. Thus, the novel methodology proposed for the isthmus cross-section computation results in a slightly more distal isthmus position but is able to assess a difference in D_{GI} between Asian and White patients comparable to literature data while being a robust automatic methodology capable of identifying the isthmus section even in case of Dorr Type C femurs.

Lastly, the height of both Asian and White patients are in agreement with the data reported in literature [10, 45, 46]. Although Asian subjects have higher BMIs compared to those described in literature [47], this is not a significant concern given the geometric nature of the present analysis, which also

suggest that the inclusion of CT images from both fresh-frozen cadaveric and living donors is of minimal concern.

For both inter- and intra-observer reliability, all parameters of interest showed high levels of agreement, with the lower boundary of the 95% confidence interval of the intraclass correlation coefficients generally exceeding 0.9, suggesting that the methodology proposed is reliable across different observers and trials. Notably, the minimum value of the lower boundary of the 95% confidence interval is 0.913 (D_{HT}) for the interobserver reliability, indicating excellent agreement between different observers. Regarding the intra-observer reliability, both observers showed good to excellent agreement across trials for all computed parameters (the minimum value of the lower boundary of the 95% confidence interval is 0.852).

The Passing-Bablok regression showed that for all parameters of interest, the slope and intercept confidence intervals contained one and zero respectively, suggesting that the results derived from automatically picked landmarks are equivalent to those computed from manually selected ones.

The main limitation of the study is the absence of anatomies from revision cases, that is, the potential modification of the anatomy due to previous implant failure was not taken into account. Nevertheless, the focus of the study is the isthmus region and, considering that a primary stem usually achieves fixation proximally, this part of the femoral canal should not be affected by previous implant failure. Another limitation of this study is its focus on modular stems, as the plane where angle α lies was not analyzed. This aspect is particularly relevant for monolithic designs. Su et al. [48] examined the angle between the femoral curvature and the coronal plane (banking angle), but in our case, the modular stem's ability to rotate along its distal axis allows alignment with the anatomical bowing plane, and the proximal body can be adjusted to achieve the desired head center position.

5 | Conclusion

Among all parameters considered, the correlation between α and D_{TI} is the most relevant one and should be considered in the design of a kinked revision stem to determine the best trade-off between fixation area and mechanical stability.

Regarding the difference between Asian and White patients found for D_{HI}, and the correlation between α and D_{HI}, they could have no practical effect in case of modular stem. On the other hand, all other parameters analysed have neither significant statistical correlation/difference nor practical impact on the design. This information is, even so, of great importance since it can induce a reduction of the design variables, thus leading to a more effective design process.

These findings should be an indication for the development of a kinked revision stem capable to achieve, in case of curved femur morphologies, optimal fixation in the isthmus region while properly aligning to the proximal femoral canal axis thus avoiding three-point fixation.

Author Contributions

The following authors have made substantial contributions to the conception and design of the study: Marco Zucchet, Cristiano Pizzamiglio, Beat Schmutz, and Michele Pressacco. Acquisition of data: Marco Zucchet, Cristiano Pizzamiglio, Beat Schmutz, and Chong Bum Chang. Development of the methodology: Marco Zucchet and Cristiano Pizzamiglio. Development of the software application: Cristiano Pizzamiglio. Analysis of data: Cristiano Pizzamiglio. Interpretation of data: Marco Zucchet, Cristiano Pizzamiglio. Drafting the article Marco Zucchet, Cristiano Pizzamiglio, Beat Schmutz. Revising for important intellectual content: Beat Schmutz, Jung-Wee Park, Michele Pressacco and final approval of the version to be submitted: Marco Zucchet, Cristiano Pizzamiglio, Beat Schmutz, Chong Bum Chang, Jung-Wee Park, Michele Pressacco.

Acknowledgments

LimaCorporate (now Enovis) provided funding for the acquisition of the CT images used in the study. Beat Schmutz received funding from LimaCorporate (now Enovis) for an initial pilot morphometric analysis. Marco Zucchet, Cristiano Pizzamiglio and Michele Pressacco are employees of LimaCorporate (now Enovis). Beat Schmutz and Chong Bum Chang provided and/or provide LimaCorporate (now Enovis) with consulting services. Jung-Wee Park declares that he does not have any competing interests.

Data Availability Statement

The datasets generated and/or analysed during the current study are not publicly available due to confidentiality reasons but may be available from the corresponding author on reasonable request. The request shall be considered reasonable if it comes from universities and/or research institutions and it is made for research and educational purposes, with the explicit exclusion of any, direct or indirect, commercial use of the mentioned datasets.

References

1. J. T. Evans, J. P. Evans, R. W. Walker, A. W. Blom, M. R. Whitehouse, and A. Sayers, "How Long Does a Hip Replacement Last? A Systematic Review and Meta-Analysis of Case Series and National Registry Reports With More Than 15 Years of Follow-Up," *Lancet* 393, no. 10172 (2019): 647–654, https://doi.org/10.1016/S0140-6736(18)31665-9.

2. AOA, Australian Orthopaedic Association National Joint Replacement Registry. Revision of Hip and Knee Arthroplasty: Supplementary Report in Hip, Knee & Shoulder Arthroplasty: 2022 Annual Report (AOA, 2022): 125, https://aoanjrr.sahmri.com/documents/10180/732931/2022+Revision+of+Hip+and+Knee+Arthroplasty+SR.pdf/e0d946e1-439a-07ff-0330-284d1f15c555?version=1.0&t=1664538343700&download=false.

3. D. F. Amanatullah, J. L. Howard, H. Siman, R. T. Trousdale, T. M. Mabry, and D. J. Berry, "Revision Total Hip Arthroplasty in Patients With Extensive Proximal Femoral Bone Loss Using a Fluted Tapered Modular Femoral Component," *Bone & Joint Journal* 97, no. 3 (2015): 312–317, https://doi.org/10.1302/0301-620X.97B3.34684.

4. R. Siwach, "Anthropometric Study of Proximal Femur Geometry and Its Clinical Application," *Annals of the National Academy of Medical Sciences (India)* 54, no. 4 (2018): 203–215, https://doi.org/10.1055/s-0040-1712831.

5. T. Wuestemann, S. G. Hoare, A. Petersik, et al., "Bone Morphology of the Proximal Femoral Canal: Ethnicity Related Differences and the Influence on Cementless Tapered Wedge Stem Designs," *HIP International* 31, no. 4 (2021): 482–491, https://doi.org/10.1177/1120700019895458.

6. M. Bozkurt, S. Gursoy, N. Shohat, M. E. Simsek, M. Akkaya, and J. Parvizi, "Definition of a Novel Proximal Femur Classification in the Sagittal Plane According to the Femur Morphometric Analysis,"

Journal of Arthroplasty 34, no. 7 (2019): 1502–1508, https://doi.org/10.1016/j.arth.2019.03.005.

7. M. Carmona, C. Tzioupis, S. LiArno, A. Faizan, J. N. Argenson, and M. Ollivier, "Upper Femur Anatomy Depends on Age and Gender: A Three-Dimensional Computed Tomography Comparative Bone Morphometric Analysis of 628 Healthy Patients' Hips," *Journal of Arthroplasty* 34, no. 10 (2019): 2487–2493, https://doi.org/10.1016/j.arth.2019.05.036.

8. P. C. Noble, J. W. Alexander, L. J. Lindahl, D. T. Yew, W. M. Granberry, and H. S. Tullos, "The Anatomic Basis of Femoral Component Design," *Clinical Orthopaedics and Related Research* 235 (1988): 148–165, https://doi.org/10.1097/00003086-198810000-00015.

9. F. Canovas, S. Putman, L. Dagneaux, L. Chadli, and P. Le Béguec, "Cementless Revision Femoral Stems Application of Press-Fit Principles and Clinical Outcomes," *International Orthopaedics* 43 (2019): 2261–2267, https://doi.org/10.1007/s00264-018-4265-4.

10. D. M. Thiesen, D. Ntalos, A. Korthaus, A. Petersik, K. H. Frosch, and M. J. Hartel, "A Comparison Between Asians and Caucasians in the Dimensions of the Femoral Isthmus Based on a 3D-CT Analysis of 1189 Adult Femurs," *European Journal of Trauma and Emergency Surgery* 48 (2021): 2379–2386, https://doi.org/10.1007/s00068-021-01740-x.

11. Xy Su, Jx Zhao, Z. Zhao, et al., "Three-Dimensional Analysis of the Characteristics of the Femoral Canal Isthmus: An Anatomical Study," *BioMed Research International* 2015, no. 1 (2015): 459612, https://doi.org/10.1155/2015/459612.

12. F. Chen, Z. Zhao, C. Gao, et al., "Clustering of Morphological Features for Identifying Femur Cavity Subtypes With Difficulties of Intramedullary Nail Implantation," *IEEE Journal of Biomedical and Health Informatics* 22, no. 4 (2018): 1209–1217, https://doi.org/10.1109/JBHI.2017.2761980.

13. J. Wilkerson and N. D. Fernando, "Classifications in Brief: The Dorr Classification of Femoral Bone," *Clinical Orthopaedics* 478, no. 8 (1939): 1939–1944, https://doi.org/10.1097/2FCORR.0000000000001295.

14. B. Mahaisavariya, K. Sitthiseripratip, T. Tongdee, E. L. Bohez, J. Vander Sloten, and P. Oris, "Morphological Study of the Proximal Femur: A New Method Ofgeometrical Assessment Using 3-dimensional Reverse Engineering," *Medical Engineering & Physics* 24, no. 9 (2002): 617–622, https://doi.org/10.1016/S1350-4533(02)00113-3.

15. H. Shimosawa, T. Nagura, K. Harato, et al., "Variation of Three-Dimensional Femoral Bowing and Its Relation to Physical Status and Bone Mineral Density: A Study With CT," *Surgical and Radiologic Anatomy* 41 (2019): 1489–1495, https://doi.org/10.1007/s00276-019-02323-7.

16. H. J. Cho, D. S. Kwak, and I. B. Kim, "Morphometric Evaluation of Korean Femurs by Geometric Computation: Comparisons of the Sex and the Population," *BioMed Research International* 2015, no. 1 (2015): 1–9, https://doi.org/10.1155/2015/730538.

17. R. Y. Zhang, X. Y. Su, J. X. Zhao, J. T. Li, L. C. Zhang, and P. F. Tang, "Three-Dimensional Morphological Analysis of the Femoral Neck Torsion Angle—An Anatomical Study," *Journal of Orthopaedic Surgery and Research* 15 (2020): 192, https://doi.org/10.1186/s13018-020-01712-8.

18. D. Dimitriou, T. Y. Tsai, B. Yue, H. E. Rubash, Y. M. Kwon, and G. Li, "Side-to-Side Variation in Normal Femoral Morphology: 3D Ct Analysis of 122 Femurs," *Orthopaedics & Traumatology, Surgery & Research: OTSR* 102, no. 1 (2016): 91–97, https://doi.org/10.1016/j.otsr.2015.11.004.

19. J. Hu, L. Xu, M. Jing, H. Zhang, L. Wang, and X. Chen, "An Approach to Automated Measuring Morphological Parameters of Proximal Femora on Three-Dimensional Models," *International Journal of Computer Assisted Radiology and Surgery* 15 (2020): 109–118, https://doi.org/10.1007/s11548-019-02095-w.

20. N. Chantarapanich, S. Rojanasthien, B. Chernchujit, et al., "3D Cad/Reverse Engineering Technique for Assessment of Thai Morphology: Proximal Femur and Acetabulum," *Journal of Orthopaedic Science* 22, no. 4 (2017): 703–709, https://doi.org/10.1016/j.jos.2017.02.003.

21. B. Schmutz, S. Kmiec, M. E. Wullschleger, M. Altmann, and M. Schuetz, "3D Computer Graphical Anatomy Study of the Femur: A Basis for a New Nail Design," *Archives of Orthopaedic and Trauma Surgery* 137 (2017): 321–331, https://doi.org/10.1007/s00402-016-2621-7.

22. D. M. Thiesen, F. Prange, J. Berger-Groch, et al., "Femoral Antecurvation—A 3D CT Analysis of 1232 Adult Femurs," *PLoS One* 13, no. 10 (2018): e0204961, https://doi.org/10.1371/journal.pone.0204961.

23. J. Cohen, *Statistical Power Analysis for the Behavioral Sciences* (Routledge, 2013), https://doi.org/10.4324/9780203771587.

24. F. Farrokhyar, D. Reddy, R. Poolman, and M. Bhandari, "Why Perform a Priori Sample Size Calculation?," *Canadian Journal of Surgery* 56, no. 3 (2013): 207–213, https://doi.org/10.1503/cjs.018012.

25. J. Kim and B. S. Seo, "How to Calculate Sample Size and Why," *Clinics in Orthopedic Surgery* 5, no. 3 (2013): 235–242, https://doi.org/10.4055/cios.2013.5.3.235.

26. G. M. Treece, A. H. Gee, P. M. Mayhew, and K. E. S. Poole, "High Resolution Cortical Bone Thickness Measurement From Clinical Ct Data," *Medical Image Analysis* 14, no. 3 (2010): 276–290, https://doi.org/10.1016/j.media.2010.01.003.

27. G. M. Treece, K. E. S. Poole, and A. H. Gee, "Imaging the Femoral Cortex: Thickness, Density and Mass From Clinical CT," *Medical Image Analysis* 16, no. 5 (2012): 952–965, https://doi.org/10.1016/j.media.2012.02.008.

28. G. M. Treece and A. H. Gee, "Independent Measurement of Femoral Cortical Thickness and Cortical Bone Density Using Clinical CT," *Medical Image Analysis* 20, no. 1 (2015): 249–264, https://doi.org/10.1016/j.media.2014.11.012.

29. H. Hoppe, T. DeRose, T. Duchamp, J. McDonald, and W. Stuetzle, "Mesh Optimization," in *Proceedings of the 20th Annual Conference on Computer Graphics and Interactive Techniques* (1993): 19–26.

30. P. Cignoni, M. Callieri, M. Corsini, et al., "Meshlab: An Open-Source Mesh Processing Tool," in *Eurographics Italian Chapter Conference*, Vol. 2008 (Salerno, 2008): 129–136.

31. M. Luthi, T. Gerig, C. Jud, and T. Vetter, "Gaussian Process Morphable Models," *IEEE Transactions on Pattern Analysis and Machine Intelligence* 40, no. 8 (2018): 1860–1873, https://doi.org/10.1109/TPAMI.2017.2739743.

32. M. Clogenson, J. M. Duff, M. Luethi, et al., "A Statistical Shape Model of the Human Second Cervical Vertebra," *International Journal of Computer Assisted Radiology and Surgery* 10 (2015): 1097–1107, https://doi.org/10.1007/s11548-014-1121-x.

33. B. Schmutz, M. Lüthi, Y. K. Schmutz-Leong, R. Shulman, and S. Platt, "Morphological Analysis of Gissane's Angle Utilising a Statistical Shape Model of the Calcaneus," *Archives of Orthopaedic and Trauma Surgery* 141 (2021): 937–945, https://doi.org/10.1007/s00402-020-03566-5.

34. M. A. Styner, K. T. Rajamani, L. P. Nolte, et al., "Evaluation of 3D Correspondence Methods for Model Building," in Information Processing in Medical Imaging: 18th International Conference, IPMI 2003, Ambleside, UK, July 20-25, 2003. Proceedings 18. (Springer, 2003): 63–75.

35. M. Zhang, B. L. Liu, X. Z. Qi, et al., "The Three-Dimensional Morphology of Femoral Medullary Cavity in the Developmental Dysplasia of the Hip," *Frontiers in Bioengineering and Biotechnology* 9 (2021): 684832, https://doi.org/10.3389/fbioe.2021.684832.

36. M. C. M. Fischer, S. A. G. A. Grothues, J. Habor, M. de la Fuente, and K. Radermacher, "A Robust Method for Automatic Identification of Femoral Landmarks, Axes, Planes and Bone Coordinate Systems Using Surface Models," *Scientific Reports* 10, no. 1 (2020): 20859, https://doi.org/10.1038/s41598-020-77479-z.

37. T. K. Koo and M. Y. Li, "A Guideline of Selecting and Reporting Intraclass Correlation Coefficients for Reliability Research," *Journal of Chiropractic Medicine* 15, no. 2 (2016): 155–163, https://doi.org/10.1016/j.jcm.2016.02.012.

38. H. Passing and W. Bablok, "A New Biometrical Procedure for Testing the Equality of Measurements From Two Different Analytical Methods," *Application of Linear Regression Procedures for Method Comparison Studies in Clinical Chemistry, Part I. Clinical Chemistry and Laboratory Medicine* Part I (1983): 709–720, https://doi.org/10.1515/cclm.1983.21.11.709.

39. H. Jeffreys, *The Theory of Probability* (OuP, 1998), https://global.oup.com/academic/product/the-theory-of-probability-9780198503682.

40. N. M. Razali and Y. B. Wah, Power Comparisons of Shapiro-Wilk, Kolmogorov-Smirnov, Lilliefors and Anderson-Darling tests, https://api.semanticscholar.org/CorpusID:18639594.

41. F. Liang, R. Paulo, G. Molina, M. A. Clyde, and J. O. Berger, "Mixtures of G Priors for Bayesian Variable Selection," *Journal of the American Statistical Association* 103, no. 481 (2008): 410–423, https://doi.org/10.1198/016214507000001337.

42. J. N. Rouder, P. L. Speckman, D. Sun, R. D. Morey, and G. Iverson, "Bayesian T Tests for Accepting and Rejecting the Null Hypothesis," *Psychonomic Bulletin & Review* 16 (2009): 225–237, https://doi.org/10.3758/PBR.16.2.225.

43. JASP Team, JASP (Version 0.18.3)[Computer software], https://jasp-stats.org/.

44. The jamovi project, jamovi, https://www.jamovi.org (2023). (Version 2.3) [Computer Software].

45. H. S. Nam, M. H. Shin, J. M. Zmuda, et al., "Race/Ethnic Differences in Bone Mineral Densities in Older Men," *Osteoporosis International* 21 (2010): 2115–2123, https://doi.org/10.1007/s00198-010-1188-3.

46. Y. M. Song and J. Sung, "Adult Height and the Risk of Mortality in South Korean Women," *American Journal of Epidemiology* 168, no. 5 (2008): 497–505, https://doi.org/10.1093/aje/kwn187.

47. S. Eum, S. Y. Rhee, et al., "Age, Ethnic, and Sex Disparity in Body Mass Index and Waist Circumference: A Bi-National Large-Scale Study in South Korea and the United States," *Life Cycle* 3 (2023): 3, https://doi.org/10.54724/lc.2023.e4.

48. X. Y. Su, Z. Zhao, J. X. Zhao, et al., "Three-Dimensional Analysis of the Curvature of the Femoral Canal II 426 Chinese Femurs," *BioMed Research International* 2015, no. 1 (2015): 1–8, https://doi.org/10.1155/2015/318391.

Supporting Information

Additional supporting information can be found online in the Supporting Information section.

Supplementary File 1: The query entered in Google Scholar to perform the search regarding the isthmus tube and axis. **Supplementary File 2:** Validation results of the automatic landmark detection algorithm. **Supplementary File 3:** Prior and posterior distributions of the effect size δ, and the Bayes factor B_{10} robustness check for D_{HI}, D_{HT}, and D_{GI}. **Supplementary File 4:** Demographics. **Supplementary File 5:** Paramters of interest.